

Study on droplet transfer and weld quality in laser-MIG hybrid welding of 316L stainless steel

Zhongmei Gao¹ · Ping Jiang¹ · Chunming Wang² · Xinyu Shao¹ · Shengyong Pang² · Qi Zhou¹ · Xiongbin Li¹ · Yilin Wang¹

Received: 7 December 2015 / Accepted: 11 April 2016 / Published online: 26 April 2016
© Springer-Verlag London 2016

Abstract Laser-MIG hybrid welding of 316L stainless steel was carried out to investigate influence of welding process parameters, i.e., laser power (P), welding current (I), distance between laser and arc (D), and welding speed (V) on arc characteristics, droplet transfer, and weld quality. Arc characteristics and droplet transfer behavior were investigated using high-speed imaging technology. Microstructures of the joint were observed by optical microscope, and microhardness was measured by microhardness tester. The results showed that the maximum deviation angle of the arc from the wire axis decreases with the increasing laser power. Welding current played a dominant role in arc length and droplet transfer mode. Optimal weld with no spatters and humps was obtained when $P=3$ kW, $I=140$ A, $D=3$ mm, and $V=1.2$ m/min. Microstructures in the weld zone mainly consist of columnar and equiaxed dendrites. Microhardness decreased toward the center of the weld zone, increased toward the WZ boundary, and decreased sharply at the heat-affected zone (HAZ).

Keywords Laser-MIG hybrid welding · Welding process parameters · Droplet transfer · Weld appearance and geometry · Microstructure · Microhardness

1 Introduction

Austenitic stainless steels are widely used in fabrication industry for their good comprehensive performance (e.g., good corrosion resistance and superior mechanical properties). In particular, 316L austenitic stainless steel is thought to be one kind of ideal materials for the ocean environment components [1, 2] because of its good corrosion-resistant performance caused by the relative lower carbon content and added molybdenum. Austenitic stainless steel can be readily welded by arc welding [3–5] and laser welding [6–8]. However, there exist disadvantages such as large heat-affected zone (HAZ), high residual stress and distortion, low welding speed for arc welding, and bad gap-bridging ability for laser welding.

Laser-arc hybrid welding technology, which combines the advantages of laser welding including high efficiency, deep penetration, and low distortion with high gap-bridging ability of arc welding, has attracted much attention and been applied in a number of different fields [9–12]. However, appropriate welding process parameters must be selected to obtain stable welding process and high-quality weld. Thus, study of process parameters (e.g., laser power, welding current, arc voltage, distance between laser and arc, welding speed) on stability of welding process and weld quality is necessary.

Many researches have been done on stability of welding process. Stability of hybrid welding process is determined by plasma behavior and metal transfer behavior. Liu et al. [13] studied effects of relative location of laser with arc on plasma behavior and weld cross section. Foster et al. [14] used a high-speed video camera to monitor the plume in 304L stainless steel welding with a 15-kW fiber laser. Chen et al. [15] studied droplet transfer at different welding positions in CO₂ laser-metal arc gas (MAG) hybrid welding. Zhang et al. [16] denoted that the CO₂ plasma plume had a significant impact to the electrode melting, droplet transfer, and weld morphology. Zhang et al.

✉ Ping Jiang
jiangping@hust.edu.cn

¹ State Key Lab of Digital Manufacturing Equipment and Technology, School of Mechanical Science and Engineering, Huazhong University of Science and Technology, Wuhan 430074, China

² School of Materials Science and Engineering, Huazhong University of Science and Technology, Wuhan 430074, China

[17] studied effects of mutual distance and laser power on plasma behavior and metal transfer and indicated that high laser power and short distance between laser beam and arc increased the droplet detachment time. Liu et al. [18] discussed arc characteristic and droplet transfer size and velocity under different laser powers and arc powers in CO₂ laser-MAG.

Weld quality can be characterized by weld appearance and geometry, mechanical properties, and so on. Ghosal and Chaki [19] optimized penetration depth using optimization method. Moradi et al. [20] studied variation of top weld width using high-speed imaging. Wahba et al. [21] analyzed droplet transfer, spatters, and weld appearance with 100 % CO₂ shielded gas. Liu et al. [22] pointed out that with the increasing distance between laser and arc, the weld bead geometry changed from “cocktail cup” to “cone-shaped.” Sathiya et al. [23] analyzed microstructures, microhardness, tensile properties, and impact properties of 904L super austenitic stainless steel using different shielding gas mixtures. Cui et al. [24] studied microstructure and microhardness of fiber laser butt welded joint of 304 stainless steel. Residual stress, microhardness, and tensile properties of 304 stainless steel by fiber laser welding were studied by Zhang et al. [25]. Joint properties such as wetting length, intermetallic phase layer thickness, and tensile strength were discussed by Thomy and Vollertsen [26]. Serizawa et al. [27] investigated the weldability of dissimilar joint between F82H and SUS316L from microstructure and Vickers hardness. Serizawa et al. [28] studied the effect of laser beam position on mechanical properties of F82H/SUS316L butt joint welded by fiber laser.

From aforementioned literatures, stability of welding process and weld quality are affected significantly by welding process parameters in the laser-arc hybrid welding. However, studies of process parameters in laser-arc hybrid welding of 316L stainless steel have not been done systematically. Therefore, in the present paper, effects of welding process parameters on arc characteristic and droplet transfer behavior are investigated employing high-speed imaging technology. In addition, effects of process parameters on weld appearance, weld geometry, microstructure, and microhardness are analyzed. Process parameters considered in the experiment were laser power (P), welding current (I), distance between laser and arc (D), and welding speed (V).

2 Experimental procedure

2.1 Material

The base metal used in the experiment was 316L austenitic stainless steel with the dimensions of 150 mm × 75 mm × 5.5 mm. Welding surface was cleaned with acetone prior to welding. The corresponding filler wire was ER316LSi with a diameter of 1.2 mm. Table 1 shows the chemical composition of the base material and the filler wire.

2.2 Experiment equipment and welding process parameters

Figure 1 shows experiment setup and schematic drawing for the fiber laser-MIG hybrid welding. The welding system comprises an IPG YLR-4000 fiber laser system, a MIG arc welding system, and an ABB IRB4400 special robot. The focal length and focal diameter on weldment surface are 250 and 0.3 mm, respectively. The MIG welding system contained a Fronius TPS4000 inverter power supply with a maximum current of 500 A, a special wire feeder, and a Fronius VR2000 MIG welding torch. The laser welding head, wire feeder, and MIG welding torch were attached to the robot. A high-speed camera (Photofocus, Switzerland) system was used to record the images of droplet at a frame rate of 2700 f/s. A narrow-band filter with a center wavelength of 808 nm which matched the backlight source was installed in front of the camera lens to filter out most of the arc light to distinguish droplets.

Bead-on plate welding was conducted in the hybrid welding. The constant and variable welding process parameters adopted in the experiment are presented in Tables 2 and 3, respectively. In Table 3, V_f automatically matched with the welding current.

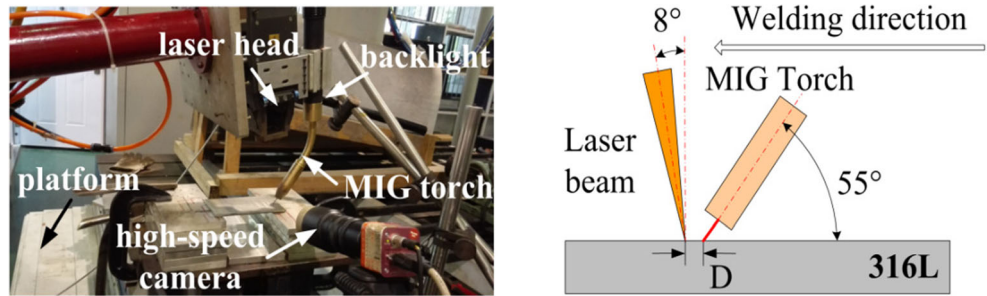
2.3 Observation and measurement

Arc and droplet can be observed directly using high-speed imaging technology. Thousands of photographs in each trial were used to average frequency of droplet transfer. Weldments were sectioned, molded, polished, and then etched by HF/HNO₃/H₂O (1:2:7 vol.) mixtures. Geometrical characteristics of weld cross section were measured utilizing a stereoscope (DH-HV315UC) and measurement software CSM1 with the precision of 1 μm. Microstructure was performed using a 3D super-depth digital microscope (KEYENCEVHX-1000C),

Table 1 Chemical composition of the base metal and the filler wire (wt%)

Material	C	Mn	P	S	Si	Ni	Cr	Mo	Cu
Base metal	≤0.03	≤2.0	≤0.045	≤0.03	≤1.0	10–14	16–18	2–3	
Filler wire	0.0213	1.74	0.027	0.009	0.83	11.66	18.6	2.5	0.26

Fig. 1 Experiment setup and schematic drawing for the hybrid welding



and microhardness test was carried out by using a microhardness machine (Wolpert Wilson 402MVD) with a loading force of 1.96 N and duration time of 15 s.

3 Theoretical background

In the hybrid laser-MIG welding, geometrical characteristics of weld cross section were affected by the hybrid heat source. The total heat input (Q) includes heat input of laser (Q_{laser}) and heat input of arc (Q_{arc}). Q can be calculated according to the following equation

$$Q = Q_{laser} + Q_{arc} = \frac{\eta_1 P_{laser} + \eta_2 UI}{V} \tag{1}$$

where P_{laser} is the laser power, U is the arc voltage, I is the welding current, η_1 and η_2 are efficiencies of laser and arc power, and V is the welding speed.

Droplet transfer mode depends on transfer distance and the resultant force exerting on the pendant droplet. Forces acting on the pendant droplet in the laser-MIG hybrid welding process are shown in Fig. 2. Detaching forces consist of gravitational force (F_g), plasma drag force (F_p), and electromagnetic force (F_{em}) which deviate from wire axis due to attraction of laser to arc. Retention forces include surface tension (F_γ) and vapor recoil force (F_v) caused by high-speed vapor jet from laser keyhole.

Table 2 Constant parameters adopted in the hybrid welding

Parameter	Value
Defocusing amount	0 mm
Angle of laser	8°
Angle of MIG torch	55°
Shielding gas	Ar
Shielding gas flow	1.0 m ³ /h
Current mode	Continuous

The forces acting on the droplet can be expressed as follows [16, 29]:

$$F_g = \frac{4}{3} \pi R^3 \rho g \tag{2}$$

$$F_p = C_D A_p \left(\frac{\rho_f v_f^2}{2} \right) \tag{3}$$

$$F_{em} = \frac{\mu_0 I^2}{4\pi} \left[\ln \frac{R \sin \theta}{r} - \frac{1}{4} - \frac{1}{1 - \cos \theta} + \frac{2}{(1 - \cos \theta)^2} \ln \frac{2}{1 + \cos \theta} \right] \tag{4}$$

$$F_\gamma = 2\pi r \gamma \tag{5}$$

$$F_v = \begin{cases} \frac{1}{4\pi R_h^2} C_D A \rho_m^2 V_0^2 \left(\frac{N_a K_B T_s^3}{M_a B_0} \right)^2 \exp(-U/T_s) \exp(-D^2/2R_h^2) & (D \leq R_h) \\ 0 & (D > R_h) \end{cases} \tag{6}$$

where R and r represent radius of droplet and the wire and ρ , ρ_f , and ρ_m represent density of droplet, the plasma, and the vapor, respectively. g is the gravitational acceleration, C_D is the drag coefficient, A_p is the projection area, v_f is the velocity of the plasma, I is the welding current, μ_0 is the permeability of free space, θ is the angle of the arc-covered area, γ is the surface tension coefficient, R_h is the distribution parameters of metal vapor, V_0 is a constant, N_a is the Avogadro's constant, K_B is the Boltzmann constant, T_s is the surface temperature of

Table 3 Variable parameters adopted in the hybrid welding

No.	P (kW)	I (A)	U (V)	V_f (m/min)	D (mm)	V (m/min)
1	3	140	18.3	4.8	3	1.2
2	2.5	140	18.3	4.8	3	1.2
3	3.5	140	18.3	4.8	3	1.2
4	3	140	18.3	4.8	2	1.2
5	3	140	18.3	4.8	1	1.2
6	3	140	18.3	4.8	3	0.65
7	3	140	18.3	4.8	3	2.1
8	3	180	20.1	6.3	3	1.2
9	3	220	23.9	7.7	3	1.2
10	3	260	26.4	8.9	3	1.2

V_f wire feeding rate, U arc voltage

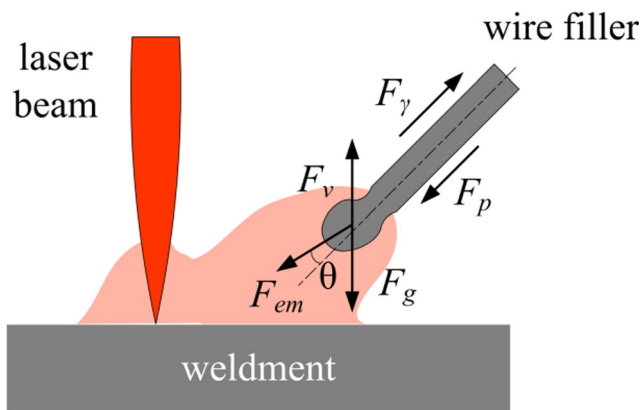


Fig. 2 Schematic drawing of forces acting on the pendant droplet in the hybrid welding

melted zone, M_a is the molecular weight, U is a calculated constant, and D is the distance between laser and arc.

4 Results and discussions

4.1 Effects of welding process parameters on arc characteristics

Laser has attraction and stabilization effect on arc in the hybrid welding. Compared with moving thermionic emission points on the weldment surface formed by arc, laser radiation point generates higher density of electrons. The laser radiation point on the weldment will be the new cathode because of the minimum voltage principle. The effects of attraction and stabilization can be demonstrated by Fig. 3. θ_1 , θ_2 , and θ_3 in Fig. 3 indicate the maximum deviation angle of the arc from the wire axis. The arc is biased toward laser, and the deviation angle decreases with the increasing laser power. Thus, it can be concluded that higher laser power makes the arc more stable. Figure 4 presents effects of welding current on arc characteristic. Anode point is formed at the bottom of the droplet. L_1 , L_2 , and L_3 in the figure refer to arc length. It can be seen that arc covering area on the weldments and arc length increase correspondingly to the increased welding current. Additionally, arc energy increases which is marked by white bright zone. In the experiment, the effects of D and V on arc characteristics are not very remarkable.

4.2 Effects of welding process parameters on droplet transfer behavior

4.2.1 Droplet transfer behavior

Figure 5 shows typical droplet transfer process observed in the experiments. Droplets are highlighted by red circles. The white areas surrounding the wire and droplet are arc plasma. Figure 5a shows the transfer process of short circuit with lower welding current, in which the droplet grows continuously until it is bigger enough to touch the molten pool. Usually, its diameter is bigger than the wire diameter. With the increasing of welding current, globular and spray transfer process will occur, as presented in Fig. 5b, c, respectively. Necking forms in the globular transfer, as can be seen in the third image of Fig. 5b. Droplets detach from the wire tip and flow to molten pool freely. From Fig. 5c, it can be observed that in spray transfer, the transfer speed is very quick and droplets look like a stream of conical liquid metal whose diameters are much smaller than the wire diameter. When the welding current is too large, the molten wire will look like a flexible liquid column swinging violently, which can be observed from Fig. 5d. The liquid column is swung out with heavy spatters, and thus, welding process is very unstable. Droplet transfer behavior is affected by other process parameters except for welding current. Effect of process parameters on droplet mode and transfer frequency will be discussed below.

4.2.2 Effects of process parameters on droplet transfer mode and frequency

High-speed images of droplet transfer and average transfer frequencies with different welding process parameters are shown in Table 4. No. 1 experiment was the base solution, in which parameters were $P=3$ kW, $I=140$ A, $D=3$ mm, and $V=1.2$ m/min.

No. 1, 2, and 3 experiments show the effect of laser power (P) on droplet transfer behavior with the constant parameters $I=140$ A, $D=3$ mm, and $V=1.2$ m/min. Droplet transfer modes were all short-circuit transfer when P increased to 3.5 from 2.5 kW. Droplet transfer frequency increased correspondingly with the increasing P .

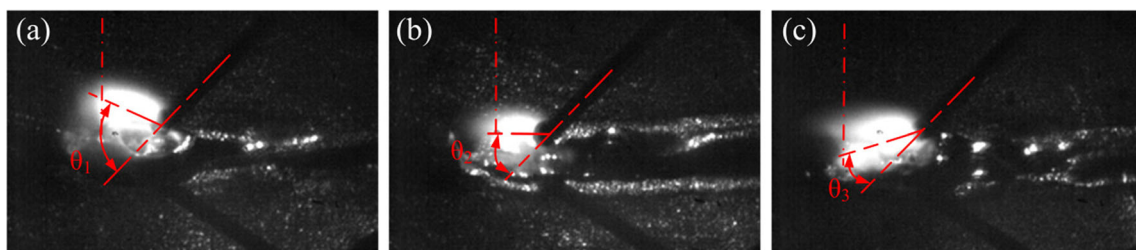


Fig. 3 Effects of laser power on arc characteristics with $I=140$ A, $D=3$ mm, and $V=1.2$ m/min and **a** $P=2.5$ kW, **b** $P=3$ kW, and **c** $P=3.5$ kW

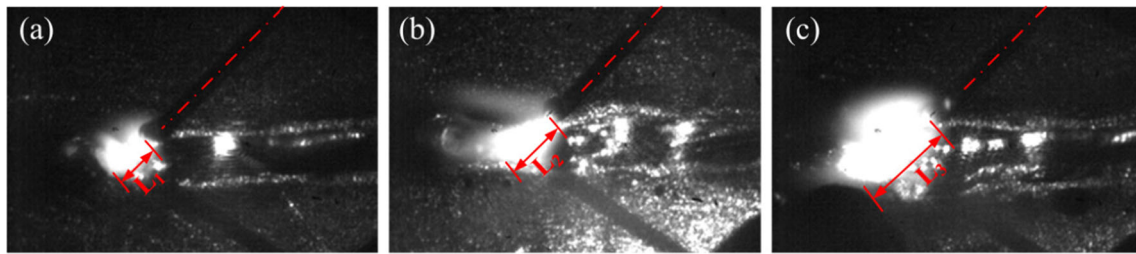


Fig. 4 Effects of welding current on arc characteristics with $P=3$ kW, $D=3$ mm, and $V=1.2$ m/min and **a** $I=140$ A, **b** $I=180$ A, and **c** $I=220$ A

No. 1, 4, and 5 experiments present the effect of distance between laser and arc (D) on droplet transfer with the constant parameters $P=3$ kW, $I=140$ A, and $V=1.2$ m/min. Droplet transfer frequency decreased with the decreasing of D , but droplet diameter increased which can be seen clearly from the photographs.

No. 1, 6, and 7 experiments show the effect of welding speed (V) on droplet transfer with the constant parameters of $P=3$ kW, $I=140$ A, and $D=3$ mm. The short-circuit transfer mode remained, and droplet transfer frequency had no obvious change with the varying V . There existed a small increment when V increased from 0.65 to 1.2 m/min and a small reduction when V increased continually to 2.1 m/min.

No. 1, 8, 9, and 10 experiments illustrate the effect of welding current (I) on droplet transfer with the constant parameters $P=3$ kW, $D=3$ mm, and $V=1.2$ m/min. When I was less than 220 A, the transfer mode was all short-circuit transfer. When I reached 220 A, the dominant transfer mode was short-circuit transfer. Meanwhile, globular and spray transfers were mixed

together. When I was set 260 A, the molten droplets look like “flexible liquid column” and swung violently though a little spray transfer occurred. And therefore, transfer frequency was not calculated. Droplet transfer frequency was the minimum when $I=180$ A.

From the results stated above, I and D have significant effect on droplet transfer behavior which can be explained as follows. According to the theoretical analysis in Sect. 3, when I increased, promotion forces F_p and F_{em} increased correspondingly. However, the short-circuit transfer mode did not change when I was less than 220 A. When I reached 220 A or more, the promotion forces F_p and F_{em} were big enough to change the transfer mode to a combination of short-circuit, globular, and spray transfers or swinging liquid column with spray transfer. The transfer distance increased when I was 180 A compared with 140 A, which can be seen from images at 0 ms in Table 5, and more time was needed for droplets to grow bigger to touch the molten pool. Thus, decreased transfer frequency and bigger droplet diameter would be seen. High-speed globular and spray

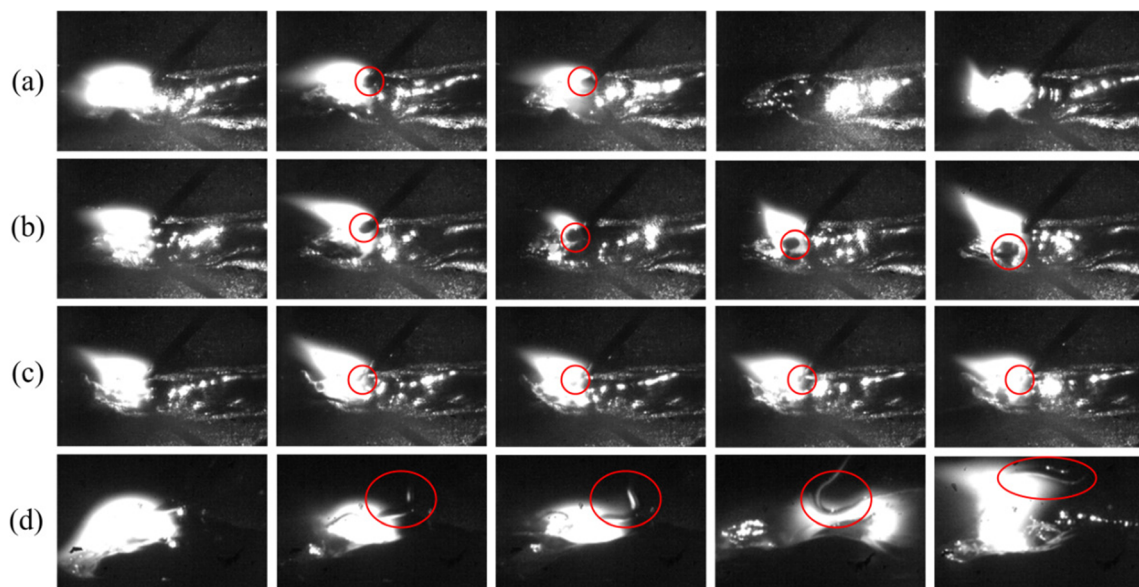


Fig. 5 Typical droplet transfer process for **a** short-circuit transfer with $I=140$ A, **b** globular transfer with $I=220$ A, **c** spray transfer with $I=220$ A, and **d** swinging liquid column with $I=260$ A

Table 4 Droplet transfer behavior for different laser powers (P)

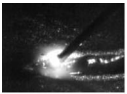
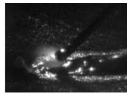
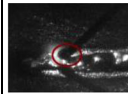
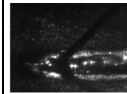
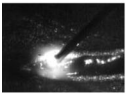
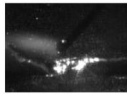
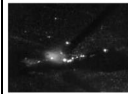
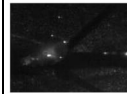
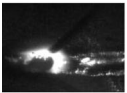

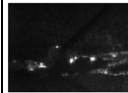
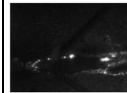

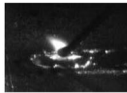
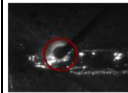

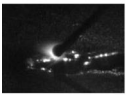
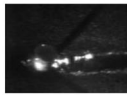

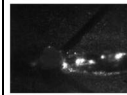
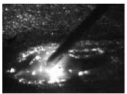
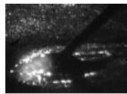
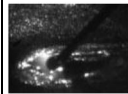
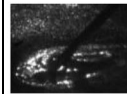
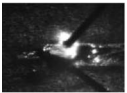

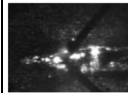
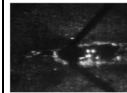
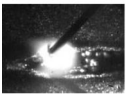


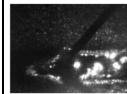

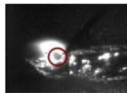

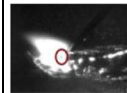


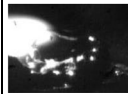
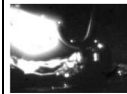
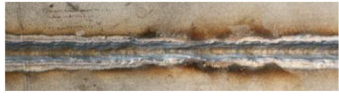
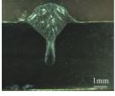

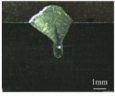

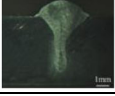


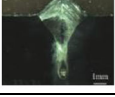


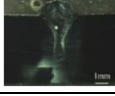






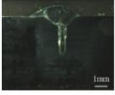


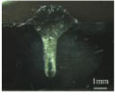
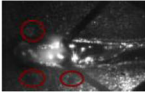


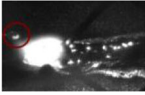
No.	Parameter		Transfer mode	Frequency (Hz)	Droplet transfer process				
1	P=3kW I=140A D=3mm V=1.2m/min		short-circuit	30					
					t=0ms	t=15ms	t=23ms	t=28ms	
2	I=140A D=3mm V=1.2m/min	P=2.5kW	short-circuit	22					
					t=0ms	t=13ms	t=50ms	t=83ms	
3		P=3.5kW	short-circuit	35					
					t=0ms	t=30ms	t=59ms	t=62ms	
4	P=3kW I=140A V=1.2m/min	D=2mm	short-circuit	27					
						t=0ms	t=13ms	t=26ms	t=40ms
5		D=1mm	short-circuit	13					
					t=17ms	t=128ms	t=204ms	t=218ms	
6	P=3kW I=140A D=3mm	V=0.65m/min	short-circuit	22					
						t=0ms	t=10ms	t=28ms	t=37ms
7		V=2.1m/min	short-circuit	26					
					t=0ms	t=16ms	t=37ms	t=51ms	
8	P=3kW D=3mm V=1.2m/min	I=180A	short-circuit	17					
						t=0ms	t=18ms	t=30ms	t=42ms
9			I=220A	short-circuit+ globular+ spray	37				
					t=0ms	t=20ms	t=25ms	t=29ms	
10		I=260A	spray+ swinging liquid column	-					
					t=0ms	t=3ms	t=4ms	t=6ms	

Table 5 Effects of welding process parameters on weld appearance

No.	Parameters		Weld appearance	Cross-section	Image with spatters
1	P=3kW D=3mm	I=140A V=1.2m/min			-
2	I=140A D=3mm	P=2.5kW			-
3	V=1.2m/min	P=3.5kW			
4	P=3kW I=140A	D=2mm			
5	V=1.2m/min	D=1mm			
6	P=3kW I=140A	V=0.65m/min	 		
7	D=3mm	V=2.1m/min			
8	P=3kW D=3mm	I=180A			
9	V=1.2m/min	I=220A			

transfers led to higher transfer frequency when I was 220 A compared with short-circuit transfer at 180 A. Decreased distance between laser and arc led to increased F_v , which prevented detachment of the droplet from wire

tip. As a result, droplet transfer frequency decreased with the decreasing D , especially when D varied from 2 to 1 mm. Meanwhile, droplet diameter increased which can be observed from the red circle zone in Table 6.

Table 6 Geometric characteristics of weld cross section

No.	DP (mm)	DP_A (mm)	BR (mm)	BW_E (mm)	WW_L (mm)	S (mm)
1	3.327	1.213	1.436	3.074	0.692	7.762
2	2.793	1.427	1.261	3.504	0.780	6.655
3	4.257	1.333	1.209	3.557	0.914	9.135
4	4.835	1.841	1.338	3.712	0.822	9.866
5	3.616	1.488	1.182	3.118	0.736	6.890
6	5.405	2.209	0	4.298	2.206	21.453
7	3.082	0.727	0.797	2.470	0.683	4.835
8	4.76	1.193	1.456	3.69	0.932	11.081
9	3.933	2.159	1.499	4.032	0.853	11.527

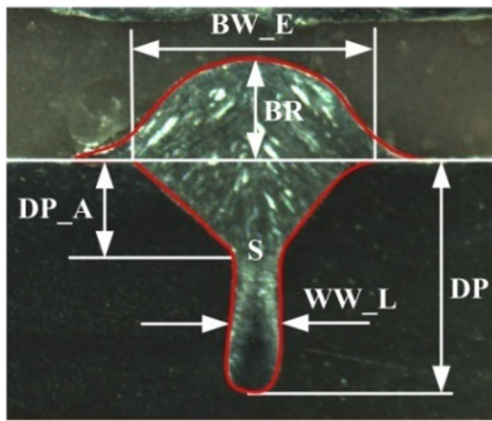


Fig. 6 Geometrical characteristics of weld cross section

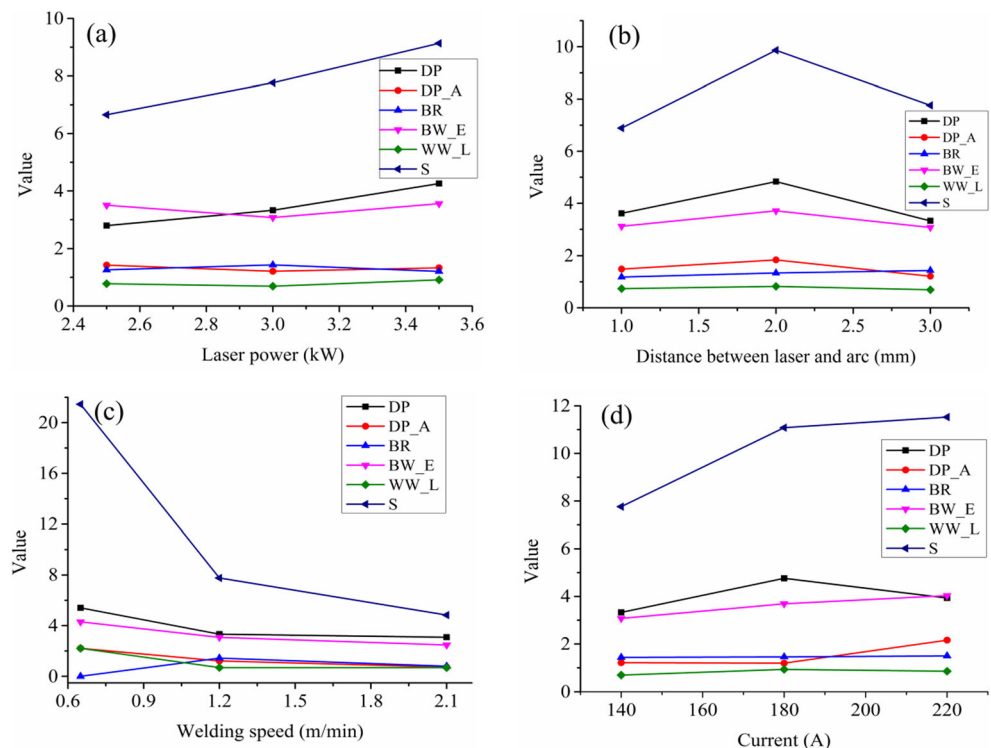
4.3 Effects of welding process parameters on weld appearance and geometry

4.3.1 Effects of welding process parameters on weld appearance

The effects of welding process parameters on weld appearance are shown in Table 5. Red circles in the table refer to the spattering droplets.

Nos. 1, 2, and 3 indicate the effect of P on weld appearance with the parameters $I = 140$ A, $D = 3$ mm, and $V = 1.2$ m/min. Beautiful weld with no spatters was obtained when P was 3 kW. Depth of penetration was very small when P was 2.5 kW which can be seen from weld cross section in the table.

Fig. 7 Effects of welding process parameters on geometrical characteristics of weld cross section



When P increased to 3.5 kW, some spatters occurred. Weld appearances were bad when D was 2 and 1 mm. Humping bead was obtained when D was set at 1 mm as a result of too slow transfer frequency. Weld appearances under different welding speed can be compared from Nos. 1, 6, and 7. Spatters were little and weld appearance was acceptable. Welding process was full penetration when V was 0.65 m/min and was partial penetration when V was 1.2 and 2.1 m/min. Weld bead subsidence occurred which can be seen from the blue circle zone of No. 8 weld cross section and high-speed images of the droplet and molten pool. Weld bead subsidence reduced the area of weld cross section and weakened the mechanical property of the joint. From Nos. 1, 8, and 9, it is observed that more spatters generated with the increasing current under the same parameters of $P = 3$ kW, $D = 3$ mm, and $V = 1.2$ m/min. The width of all the three welds was uniform, which indicated that the welding process was stable.

From the analysis of effects of process parameters on weld appearance above, the optimal welding process parameters were $P = 3$ kW, $I = 140$ A, $D = 3$ mm, and $V = 1.2$ m/min. And thus, No. 1 weld was selected for the analysis of microstructure and microhardness below.

4.3.2 Effects of welding process parameters on weld geometry

From Table 5, it can be seen that full and partial penetration occurred and weld geometry differed with different welding process parameters. The influence of welding process

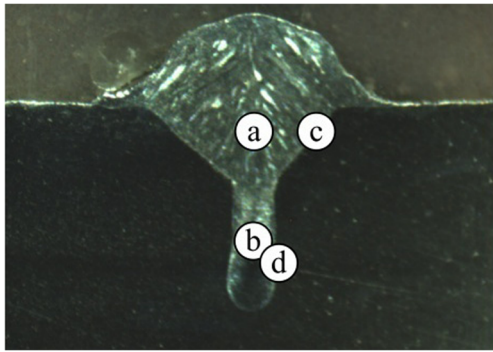


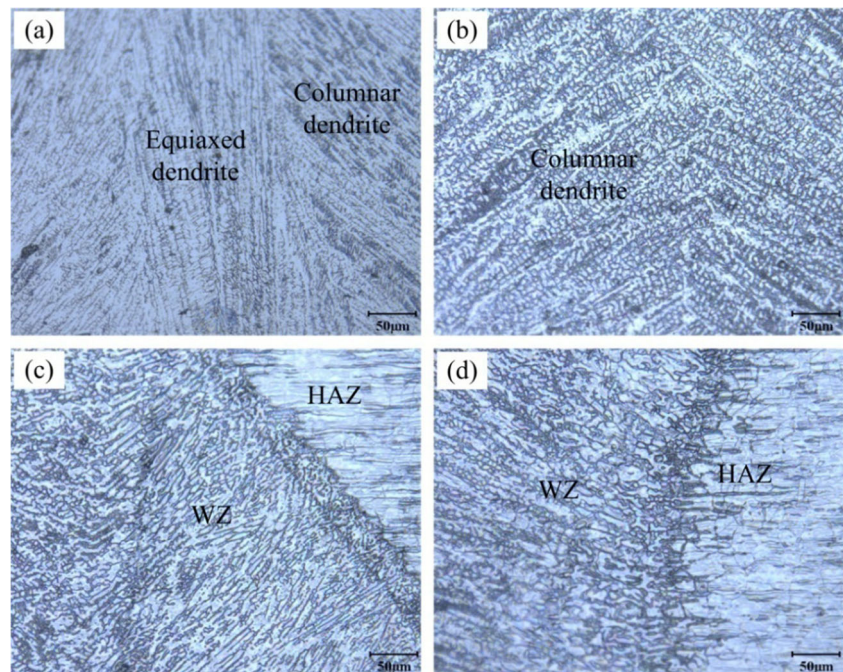
Fig. 8 Locations of the micrographs in the cross section of welded joint

parameters on weld geometry will be discussed in detail based on geometrical characteristics of weld cross section.

Figure 6 illustrates what was measured for each geometrical characteristic of weld cross section. In the figure, DP, DP_A, BW_E, WW_L, BR, and S denote depth of penetration, depth of penetration caused by arc, effective weld bead width, weld width caused by laser, bead reinforcement, and area of weld cross section, respectively. The results of experiments are listed in Table 6, and the effects of welding process parameters on geometrical characteristics of weld cross section are depicted clearly in Fig. 7.

From Fig. 7a, it can be seen that with the increasing of P from 2.5 to 3.5 kW, DP and S increased correspondingly because more laser energy input was generated. Other geometrical characteristics had little change with the variation of P , which indicated that P had little effects on them. Thus, it can be concluded that P mainly controlled DP and had little effects on other geometrical characteristics.

Fig. 9 Microstructures of No. 1 welded joint with a high magnification, see Fig. 8 for letter reference



In Fig. 7b, there were scarcely any variations for DP_A, BR, BW_E, and WW_L when D was varied from 3 to 1 mm. DP and S increased at first and then decreased. They achieved the maximum values when D was 2 mm. Therefore, the optimal distance between laser and arc was 2 mm, at which the strongest interactions between laser and arc occurred. When D was too small, vapor jet impeded transfer of droplets. Laser energy used to heat the weldment decreased because of energy absorption by droplets, and consequently, less energy input led to smaller DP and S.

The smaller the welding speed was, the larger the energy input was for both laser and arc source. From Fig. 7c, it can be observed that increased DP, DP_A, BW_E, WW_L, and S were obtained with the decreasing V . Full-penetration weld was obtained when V was 0.65 m/min. However, BR was zero in No. 6 full-penetration welding and weld bead subsidence occurred, which was not beneficial to mechanical property, e.g., tensile strength.

Figure 7d presents the effects of welding current on each geometrical characteristic of weld cross section. S increases greatly when I was increased from 140 to 180 A; however, it has hardly any change when I is increased to 220 A. BR and WW_L had no significant changes, and BW_E increased correspondingly with the increasing I . DP_A was deepest when I was 220 A; nevertheless, the deepest DP was obtained when I was 180 A. Thus, I mainly influenced BW_E, and under the same circumstance, the combined effect of laser and arc was more remarkable when I was 180 A.

From the results presented above, P and I mainly influenced DP and BW_E by energy input, and positive correlation existed between them, respectively. D played a significant role

in interactions between laser source and arc source, and the optimal D was 2 mm in the experiments. V had a positive influence on all the geometrical characteristics except for BR. Full penetration would be produced using slow welding speed, but too, slow speed would lead to weld bead subsidence.

4.4 Microstructure analysis

Figure 8 shows the locations of the micrographs taken from the optimal No. 1 weld joint. “a” and “c” refer to the center of the weld bead and interface between weld zone (WZ) and heat-affected zone (HAZ) affected by both laser and arc. “b” and “d” distinguish the keyhole zone granted by the laser source. Figure 9 shows all those micrographs. Fusion line between WZ and HAZ in Fig. 9c was more apparent than that in Fig. 9d, and HAZ in Fig. 9c was much wider because of the influence of arc source. From Fig. 9a, b, coarse serrated morphology appeared in the fusion boundary. Columnar dendrites and equiaxed dendrites can be observed in the WZ in Fig. 9a, while only columnar dendrites can be seen in the WZ in Fig. 9b. Moreover, columnar dendrites close to the fusion line grew in preferred normal-to-isotherm line direction. The microstructure can be explained as follows: the solidification mode of microstructure depends on the ratio of temperature gradient to cooling rate [30]. The ratio was the maximum in the weld boundary which favored the growth of columnar dendrites, and smaller ratio toward the center of the WZ inhibited the continuing growth of columnar dendrites and benefited equiaxed dendrites. The ratio in WZ center influenced by laser and arc was smaller than that of keyhole zone center; thereby, more equiaxed dendrites existed in Fig. 9a.

4.5 Microhardness analysis

Figure 10 shows microhardness across the weld cross section of No. 1 welded joint. Microhardness was measured at the middle

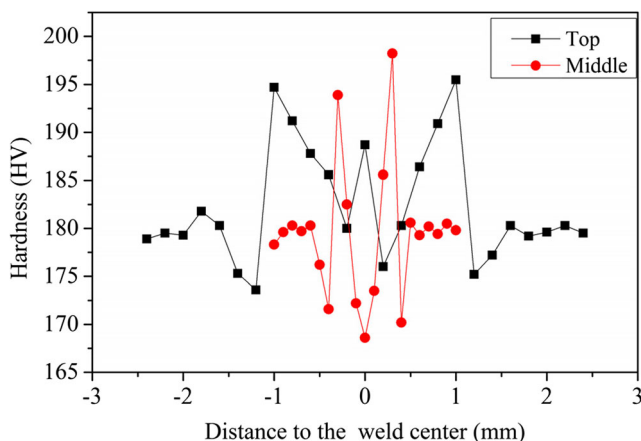


Fig. 10 Microhardness distribution across the weld cross section

with 0.1-mm intervals and at 0.5 mm below the top surface with 0.2-mm intervals. Microhardness was different from the top to the middle. Microhardness decreased toward the center of the WZ due to self-annealing effect during the cooling process. The sudden change of growth direction of columnar dendrites and little equiaxed dendrites contributed to the lowest microhardness at WZ center at the middle. However, high microhardness of WZ center at the top was attributed to the plentiful fine equiaxed dendrites. Furthermore, microhardness increased toward the WZ boundary and decreased sharply at the HAZ. HAZ microhardness was lower than the base metal microhardness due to coarse grains and material softening.

5 Conclusions

Fiber laser-MIG hybrid welding of 316L stainless steel plates was performed. Effects of welding parameters on arc characteristic, droplet transfer, weld appearance, and weld geometry were discussed. Microstructure and microhardness were analyzed as well. The main findings can be concluded as follows:

1. The maximum deviation angle of the arc from the wire axis decreases with the increasing laser power. Arc length increases with the increasing welding current. Effects of welding speed and distance between laser and arc on arc characteristics are not very remarkable.
2. Droplet transfer mode mainly depends on welding current. Droplet transfer frequency decreased firstly and then increased with the increasing welding current. It decreased with the decreasing laser power and distance between laser and arc.
3. Better weld with no spatters and humps is obtained at the parameters of $P=3$ kW, $I=140$ A, $D=3$ mm, and $V=1.2$ m/min. The optimal distance between laser and arc is 2 mm to obtain the maximum depth of penetration. Welding mode changes to full penetration from partial penetration when welding speed is 0.65 m/min.
4. Microstructures in the WZ affected by laser-MIG mainly consist of columnar and equiaxed dendrites, while only columnar dendrites can be observed in the WZ affected by laser.
5. Microhardness decreased toward the center of the WZ, increased toward the WZ boundary, and decreased sharply at the HAZ. Higher microhardness at the top of WZ center is attributed to plentiful fine equiaxed dendrites.

Acknowledgments The authors appreciate the financial support from the National Basic Research Program (973 Program) of China under Grant No. 2014CB046703, the National Natural Science Foundation of China (NSFC) under Grant Nos. 51323009 and 51421062, and the Fundamental Research Funds for the Central Universities, HUST: Grant No. 2014TS040. The authors would also like to thank the anonymous referees for their valuable comments.

References

- Traverso P, Canepa E (2014) A review of studies on corrosion of metals and alloys in deep-sea environment. *Ocean Eng* 87:10–15. doi:10.1016/j.oceaneng.2014.05.003
- Wang ZY, Cong Y, Zhang T (2014) Effect of hydrostatic pressure on the pitting corrosion behavior of 316L stainless steel. *Int J Electrochem Sci* 9:778–798
- Elmesalamy A, Francis JA, Li L (2014) A comparison of residual stresses in multi pass narrow gap laser welds and gas-tungsten arc welds in AISI 316L stainless steel. *Int J Pres Vessel Pip* 113:49–59. doi:10.1016/j.ijvp.2013.11.002
- Buddu RK, Chauhan N, Raole PM (2014) Mechanical properties and microstructural investigations of TIG welded 40mm and 60mm thick SS 316L samples for fusion reactor vacuum vessel applications. *Fusion Eng Des* 89(12):3149–3158. doi:10.1016/j.fusengdes.2014.10.006
- Duan ZL, Qin RY, He G (2014) Mass transfer and weld appearance of 316L stainless steel covered electrode during shielded metal arc welding. *Metall Mater Trans A* 45(2):843–853. doi:10.1007/s11661-013-2001-7
- Chukkan JR, Vasudevan M, Muthukumaran S, Kumar RR, Chandrasekhar N (2015) Simulation of laser butt welding of AISI 316L stainless steel sheet using various heat sources and experimental validation. *J Mater Process Technol* 219:48–59. doi:10.1016/j.jmatprotec.2014.12.008
- Tomashchuk I, Grevey D, Sallamand P (2015) Dissimilar laser welding of AISI 316L stainless steel to Ti6-Al4-6V alloy via pure vanadium interlayer. *Mater Sci Eng A* 622:37–45. doi:10.1016/j.msea.2014.10.084
- Köse C, Kaçar R, Zorba AP, Bağirova M, Allahverdiyev AM (2016) The effect of CO₂ laser beam welded AISI 316L austenitic stainless steel on the viability of fibroblast cells, in vitro. *Mater Sci Eng C* 60:211–218. doi:10.1016/j.msec.2015.11.035
- Ribic B, Palmer TA, DebRoy T (2009) Problems and issues in laser-arc hybrid welding. *Int Mater Rev* 54(4):223–244. doi:10.1179/174328009X411163
- Cao X, Wanjara P, Huang J, Munro C, Nolting A (2011) Hybrid fiber laser-arc welding of thick section high strength low alloy steel. *Mater Des* 32(6):3399–3413. doi:10.1016/j.matdes.2011.02.002
- Casalino G, Campanelli SL, Ludovico AD (2013) Laser-arc hybrid welding of wrought to selective laser molten stainless steel (2014). *Int J Adv Manuf Technol* 68(1–4):209–216. doi:10.1007/s00170-012-4721-z
- Liu W, Ma J, Yang G, Kovacevic R (2014) Hybrid laser-arc welding of advanced high-strength steel. *J Mater Process Technol* 214(12):2823–2833. doi:10.1016/j.jmatprotec.2014.06.018
- Liu LM, Yuan ST, Li CB (2012) Effect of relative location of laser beam and TIG arc in different hybrid welding modes. *Sci Technol Weld Join* 17:441–446. doi:10.1179/1362171812Y.0000000033
- Foster M, Beaulieu R, Blais L, Caron G, Langlois M (2013) Experimental investigation on stainless steel welding with a 15 kW fibre laser. *Can J Phys* 92:246–252. doi:10.1139/cjp-2012-0558
- Chen Y, Feng J, Li L, Li Y, Chang S (2013) Effects of welding positions on droplet transfer in CO₂ laser-MAG hybrid welding. *Int J Adv Manuf Technol* 68(5–8):1351–1359. doi:10.1007/s00170-013-4926-9
- Zhang W, Hua XM, Liao W, Li F, Wang M (2014) Study of metal transfer in CO₂ laser + GMAW-P hybrid welding using argon-helium mixtures. *Opt Laser Technol* 56:158–166. doi:10.1016/j.optlastec.2013.08.006
- Zhang W, Hua XM, Liao W, Li F, Wang M (2014) Behavior of the plasma characteristic and droplet transfer in CO₂ laser-GMAW-P hybrid welding. *Int J Adv Manuf Technol* 72:935–942. doi:10.1007/s00170-014-5731-9
- Liu SY, Liu FD, Xu CY, Zhang H (2013) Experimental investigation on arc characteristic and droplet transfer in CO₂ laser-metal arc gas (MAG) hybrid welding. *Int J Heat Mass Transf* 62:604–611. doi:10.1016/j.ijheatmasstransfer.2013.03.051
- Ghosal S, Chaki S (2010) Estimation and optimization of depth of penetration in hybrid CO₂ laser-MIG welding using ANN-optimization hybrid model. *Int J Adv Manuf Technol* 47(9):1149–1157. doi:10.1007/s00170-009-2234-1
- Moradi M, Ghoreishi M, Frostevarg J, Kaplan AFH (2013) An investigation on stability of laser hybrid arc welding. *Opt Lasers Eng* 51:481–487. doi:10.1016/j.optlaseng.2012.10.016
- Wahba M, Mizutani M, Katayama S (2015) Hybrid welding with fiber laser and CO₂ gas shielded arc. *J Mater Process Technol* 221:146–153. doi:10.1016/j.jmatprotec.2015.02.004
- Liu SY, Liu FD, Zhang H, Shi Y (2012) Analysis of droplet transfer mode and forming process of weld bead in CO₂ laser-MAG hybrid welding process. *Opt Laser Technol* 44:1019–1025. doi:10.1016/j.optlastec.2011.10.016
- Sathiya P, Mishra MK, Shanmugarajan B (2012) Effect of shielding gases on microstructure and mechanical properties of super austenitic stainless steel by hybrid welding. *Mater Des* 33:203–212. doi:10.1016/j.matdes.2011.06.065
- Cui CY, Cui XG, Ren XD, Liu TT, Hu JD, Wang YM (2013) Microstructure and microhardness of fiber laser butt welded joint of stainless steel plates. *Mater Des* 49:761–765. doi:10.1016/j.matdes.2013.02.059
- Zhang L, Lu JZ, Luo KY, Feng AX, Dai FZ, Zhong JS, Luo M, Zhang YK (2013) Residual stress, micro-hardness and tensile properties of ANSI 304 stainless steel thick sheet by fiber laser welding. *Mater Sci Eng A* 561:136–144. doi:10.1016/j.msea.2012.11.001
- Thomy C, Vollertsen F (2012) Laser-MIG hybrid welding of aluminium to steel—effect of process parameters on joint properties. *Weld World* 56:124–132
- Serizawa H, Mori D, Shirai Y, Ogiwara H, Mori H (2013) Weldability of dissimilar joint between F82H and SUS316L under fiber laser welding. *Fusion Eng Des* 88:2466–2470. doi:10.1016/j.fusengdes.2013.03.041
- Serizawa H, Mori D, Ogiwara H, Mori H (2014) Effect of laser beam position on mechanical properties of F82H/SUS316L butt-joint welded by fiber laser. *Fusion Eng Des* 89:1764–1768. doi:10.1016/j.fusengdes.2013.12.003
- Kim YS, Eagar TW (1993) Numerical analysis of metal transfer in gas metal arc welding. *Weld J* 72(6):269–277
- Yilbas BS, Akhtar S (2013) Laser welding of AISI 316 steel: microstructural and stress analysis. *J Manuf Sci Eng* 135(3):031018. doi:10.1115/1.4024155